Article

Dynamic spatial progression of isolated lithium during battery operations

Fang Liu[1], Rong Xu[1], Yecun Wu[2], David Thomas Boyle[3], Ankun Yang[1], Jinwei Xu[1], Yangying Zhu[1], Yusheng Ye[1], Zhiao Yu[4], Zewen Zhang[1], Xin Xiao[1], Wenxiao Huang[1], Hansen Wang[1], Hao Chen[1] & Yi Cui[1,5] ✉

The increasing demand for next-generation energy storage systems necessitates the development of high-performance lithium batteries[1-3]. Unfortunately, current Li anodes exhibit rapid capacity decay and a short cycle life[4-6], owing to the continuous generation of solid electrolyte interface[7,8] and isolated Li (i-Li)[9-11]. The formation of i-Li during the nonuniform dissolution of Li dendrites[12] leads to a substantial capacity loss in lithium batteries under most testing conditions[13]. Because i-Li loses electrical connection with the current collector, it has been considered electrochemically inactive or 'dead' in batteries[14,15]. Contradicting this commonly accepted presumption, here we show that i-Li is highly responsive to battery operations, owing to its dynamic polarization to the electric field in the electrolyte. Simultaneous Li deposition and dissolution occurs on two ends of the i-Li, leading to its spatial progression toward the cathode (anode) during charge (discharge). Revealed by our simulation results, the progression rate of i-Li is mainly affected by its length, orientation and the applied current density. Moreover, we successfully demonstrate the recovery of i-Li in Cu−Li cells with >100% Coulombic efficiency and realize $LiNi_{0.5}Mn_{0.3}Co_{0.2}O_2$ (NMC)−Li full cells with extended cycle life.

Isolated Li (i-Li), the metallic Li that loses electrical connection with the current collector, has been generally perceived as electrochemically inactive or 'dead' in batteries[14,15]. Several strategies have been focused on suppressing its formation by optimizing the electrolyte chemistry[16-18], interfacial properties[19-21] and electrode architecture[22-24]. Although substantial improvements have been achieved from an engineering perspective, the formation and accumulation of i-Li remains a primary cause of capacity loss in most lithium batteries[13]. We note that the generation of i-Li and its detrimental consequences are not limited to lithium batteries. Graphite anodes in lithium-ion batteries could also form i-Li under fast-charging[25] and overcharging[26].

Here we ask whether i-Li could be responsive to electrochemical processes, or whether it is really 'dead' as commonly perceived. In a typical Li-based battery, the lithium salt in the electrolyte dissociates into cations and anions, which carry ionic current between the electrodes during battery operations. This ionic current would create an electric potential gradient ($\nabla\phi_l$) in the electrolyte. Although i-Li loses electrical connection with the current collector, it is exposed to the electric field in the electrolyte. As a result, the charge distribution on the i-Li will be altered to screen the external electric field, namely the polarization of i-Li (Fig. 1). The accumulated positive/negative charges will disrupt the equilibrium state at the i-Li/electrolyte interface and induce charge transfer reactions on i-Li. The driving force of such responses is the potential difference (or overpotential η) across the interface, which can be described as

$$\eta = \phi_{Li} - \phi_l - E_{eq}, \tag{1}$$

where ϕ_{Li}, ϕ_l and E_{eq} represent the electric potential of Li (constant), the local electrolyte potential and the equilibrium potential of Li deposition/dissolution reactions, respectively[27,28].

During charge, the electric field points from the positive electrode to the negative electrode (Li$^+$ moves from the positive electrode to the negative electrode). The overpotential at the end of i-Li near the positive electrode turns negative ($\eta < 0$), causing Li deposition on the i-Li. Meanwhile, the overpotential at the other end turns positive ($\eta > 0$), leading to Li dissolution (Fig. 1b). The charge neutrality of i-Li is maintained by the transport of electrons from one end to the other. The net outcome is a spatial progression of i-Li toward the positive electrode (left). When the direction of the electric field is reversed during discharge (Li$^+$ moves from the negative electrode to the positive electrode), i-Li evolves toward the negative electrode (right) (Fig. 1c).

To determine whether i-Li is electrochemically active during cycling or not, we fabricated an optical cell with an i-Li island between $LiNi_{0.5}Mn_{0.3}Co_{0.2}O_2$ (NMC) and Li electrodes (Fig. 2a, Extended Data Fig. 1a). This cell configuration captures in real time the morphological changes of the i-Li island during electrochemical processes. Although
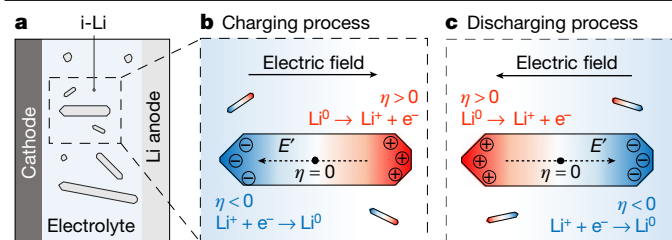
Article

Fig. 1 | Dynamic polarization of i-Li under an electric field. a, Schematic illustration of the electric-field-induced charge separation on i-Li. **b**, **c**, The resultant charge transfer reactions during charge (**b**) and discharge (**c**). Blue (red) represents the accumulation of negative (positive) charges on the i-Li.

the dimensions of the i-Li island are much larger compared to that of i-Li filaments, its evolution would be highly representative of, if not equivalent to, that of an i-Li filament because of the compositional similarity. After depositing Li on the island (Extended Data Fig. 1b), we started to charge–discharge the outer NMC–Li cell (Fig. 2b). During the charging process, we observed notable but different morphological changes on its two ends (Fig. 2c). The part of the i-Li island close to the Li electrode dissolves and produces black solid electrolyte interphase (SEI) residuals on the Cu substrate, which are composed of Li_2O, LiF, and some organic moieties (C–C, O–C=O, C–O) (Extended Data Fig. 2a). Meanwhile, metallic Li filaments with similar SEI compositions (Extended Data Fig. 2b) deposit on the other side of the island near the NMC electrode. The continuous asymmetric dissolution/deposition leads to a sizeable spatial progression of i-Li toward the cathode (a net motion >30 μm in 3 h). Similar spatial progressions have also been observed with micrometre-sized, electrochemically formed 'dead Li' (Extended Data Fig. 3). We note that the distance between newly formed 'dead Li' and active electrode surface (Li/current collector) can be within 1–2 μm or just a few hundred nanometres[12,13]. In this context, although the net motion of i-Li filaments in a real cell configuration may be less than that in the optical cells, it can be sufficient for the recovery of i-Li. During discharge, the direction of spatial progression is reversed and the i-Li island evolved toward the anode (Fig. 2d).

In addition, we developed an electrochemical model to understand the transport of Li^+ at the i-Li/electrolyte interface during the spatial

progression of i-Li. The electrolyte reservoir between the NMC and Li electrodes is depicted as a rectangular box in Fig. 2e, f, and the current density on the island surface is illustrated with a three-dimensional heatmap. During charge, the NMC side has a higher electrolyte potential than the Li side (Extended Data Fig. 4a) and this electrolyte potential gradient induces the charge transfer reactions at the i-Li/electrolyte interface. The rectangular i-Li island in the centre gradually evolves into a wedge shape and becomes closer to the NMC electrode (Fig. 2e), which is consistent with our experimental observations (Fig. 2c). The local consumption (generation) of Li^+ on the i-Li island drives the Li^+ transport from the NMC electrode to the i-Li island (i-Li island to the Li electrode). Moreover, the Li^+ flux near the island is 3–4 times higher than that near the NMC/Li electrode (Fig. 2e), indicating faster electrochemical kinetics. During discharge, the electrolyte potential gradient is reversed (Extended Data Fig. 4b), and the i-Li island evolves toward the Li electrode (Fig. 2f).

In addition to the optical cells, we also designed and customized a four-electrode set-up to measure the electrolyte potential gradient in coin cell configurations. The set-up consists of an NMC cathode, two Cu mesh electrodes and a Li anode (Fig. 3a). We pre-deposited Li onto both Cu meshes to minimize voltage fluctuations and these two electrodes are referred to as Cu/Li (A/B). Within the cell, they are electrically separated by a 12-μm-thick polypropylene (PP) separator. Because these two electrodes are not connected to the external circuit, their potential difference (V_{AB}) represents the electrolyte potential difference over a 12-μm distance. To obtain the correlation between V_{AB} and current density, we increased the current stepwise from 0.15 to 0.30, 0.60 and 0.88 mA cm^{-2} with resting steps in between and recorded V_{AB} under each condition. The NMC–Li cell exhibits a typical voltage profile during charge, and the cell voltage (V_{cell}) returns to equilibrium potential during resting (Fig. 3b). In the meantime, V_{AB} remains nearly constant during galvanostatic charging and immediately dropped to approximately 0 mV when resting starts (Fig. 3c). The electrolyte potential at Cu/Li (A) (near the NMC) is always higher than that of Cu/Li (B) (near the Li), consistent with our previous analysis. As the current density increases from 0.15 to 0.88 mA cm^{-2}, the electrolyte potential difference (V_{AB}) increases accordingly, from 11.9 to 64.4 mV.

We further adapted the previous electrochemical model to investigate the overpotentials experienced by a filament of i-Li in a coin cell configuration. Consistently, the overpotential is positive on the side of
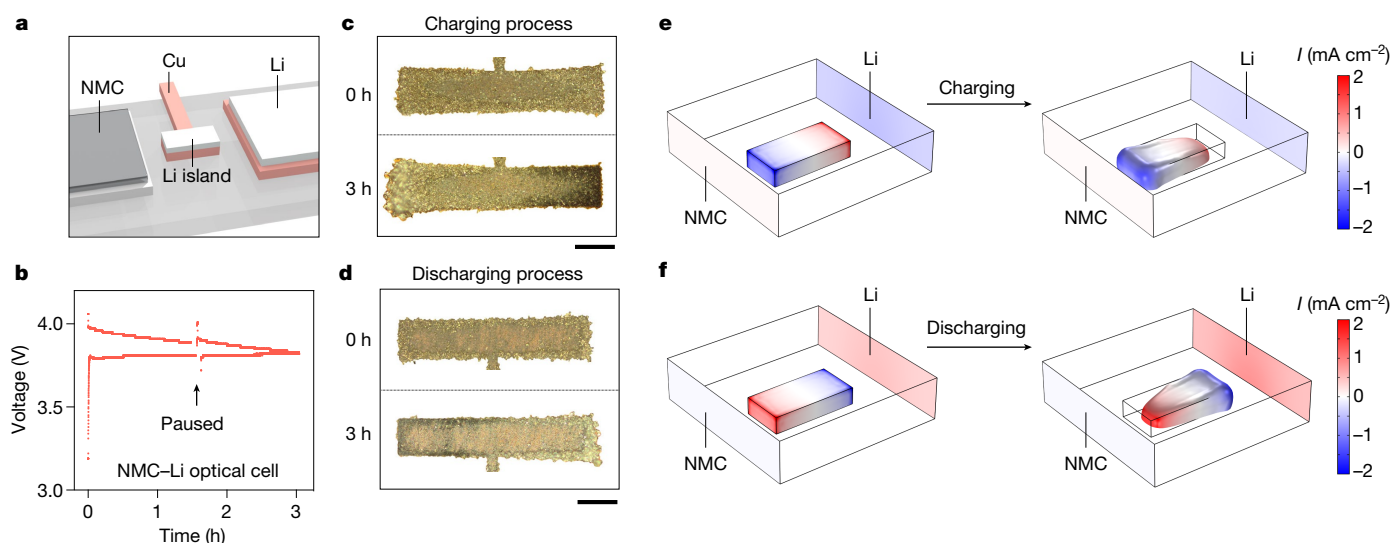

Fig. 2 | Morphological evolution of the i-Li island. a, Configuration of the optical cell with an i-Li island between the NMC and Li electrodes. **b**, Overlayed voltage profiles of two NMC–Li optical cells during the first 3-h charge–discharge. **c**, **d**, Optical images of one Li island at the initial state (t = 0 h) and

intermediate state (t = 3 h) during charge (**c**) and discharge (**d**). **e**, **f**, The current density on the i-Li surface at initial state (t = 100 s) and intermediate state (t = 2 h) during charge (**e**) and discharge (**f**). Scale bars in **c**, **d** are 100 μm.
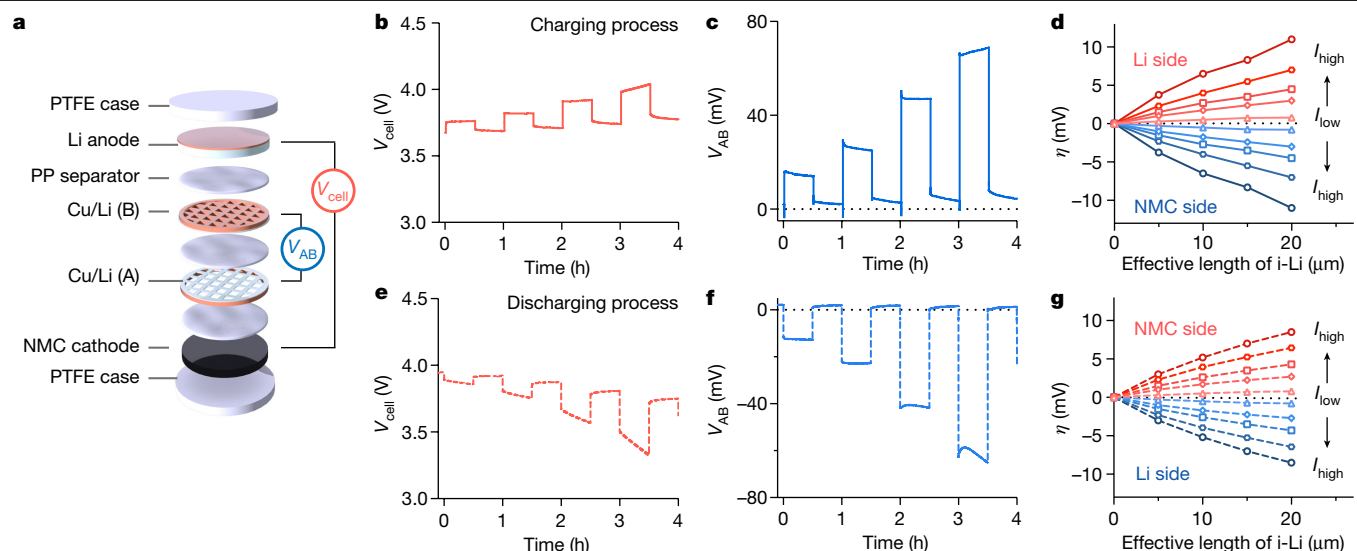
Fig. 3 | Quantification of the overpotentials on i-Li in coin cells.
a, Configuration of a NMC–Li cell with two Cu/Li electrodes in between.
b, **c**, **e**, **f**, Voltage–time profiles of the NMC–Li cell (**b**, **e**), and V_{AB} (**c**, **f**) during the intermittent charging (**b**, **c**) and discharging (**e**, **f**) processes. The current density is increased stepwise at values of 0.15, 0.30, 0.60 and 0.88 mA cm^{-2}.

d, **g**, Overpotentials at the two ends of i-Li (**d**, Li side; **g**, NMC side) for different lengths L at current densities of 0.30, 0.90, 1.50, 2.25 and 3.00 mA cm^{-2}. Solid lines represent the charging process and dashed lines show the discharging process.

the i-Li close to the Li electrode and negative near the NMC electrode during charge (Fig. 3d). The charge densities on the two ends of the i-Li are equivalent, owing to charge neutrality. The overpotential is closely correlated with the length of the i-Li, but independent of its width. Under a charging current of 1.5 mA cm^{-2}, the overpotential at the end of a 20-µm-long filament of i-Li is three times higher than that of a filament that is 5-µm long with the same width (Fig. 3d). Meanwhile, i-Li filaments with the same length but different widths (0.3, 0.5 and 1 µm) experience similar overpotentials at their end (Extended Data Fig. 5a). Unless specified, i-Li filaments in the model are 0.5 µm in width. Moreover, the overpotential closely correlates with the applied current density. For instance, when the current density increases from 0.3 to 3 mA cm^{-2}, the overpotential at the end of a 20-µm-long i-Li filament increases from 0.8 to 11 mV. Moreover, when the current density further rises to 4.5 mA cm^{-2} and Li$^+$ depletion occurs on the cathode side, the overpotential can reach 33 mV (Extended Data Fig. 5b). Although the magnitude of the electrolyte potential is not as large as that of the cell potential, its gradient can still result in a substantial overpotential on i-Li to drive Li plating/stripping, especially under high current densities.

During discharge, the direction of the electric field direction is reversed, pointing from the Li electrode to the NMC electrode. As Li$^+$ cations are consumed at the NMC electrode and generated at the Li electrode, Cu/Li (B) has a higher electric potential than that of Cu/Li (A) (Fig. 3e, f). The overpotential at the i-Li/electrolyte interface near the NMC side becomes positive, and turns negative near the Li side (Fig. 3g), thereby driving the progression of i-Li toward the Li anode. Similar to the charging process, the overpotential on i-Li increases with the length of i-Li and the applied current density. Extended Data Fig. 5c further compares the local current density at the end of the i-Li and Li bulk electrodes under various current densities. In general, the charge transfer rate on Li bulk electrode is higher than that on the 5-µm-long i-Li but lower than that on the 20-µm-long i-Li during discharge. Additionally, the progression rate of i-Li toward the Li anode is also influenced by its orientation. We found that the i-Li filaments in all directions exhibit a notable progression over time, and the ones along the direction of the electric field migrate faster than others (Extended Data Fig. 5d).

The progression of i-Li toward the anode during discharge offers an opportunity for its reconnection and recovery. Here we used the voltage difference between graphite and metallic Li to monitor the distance

of the progression of i-Li in coin cells. A Cu/Li electrode is used as the i-Li and inserted between the NMC and graphite electrodes (denoted as G) at a fully charged state. To allow the free growth of Li, we used a polyimide membrane with 200-µm pores as the separator. The NMC–G cell without i-Li presents a representative discharge profile, delivering a specific capacity of 109.6 mAh g^{-1} (Fig. 4a). Given that the polyimide membrane partially blocks the ion transport between two electrodes, the cells with polyimide separators exhibit lower capacity than cells with polypropylene separators (Extended Data Fig. 6a) and in the literature[29]. By contrast, the cell with i-Li displays more complex electrochemical behaviours, which can be categorized into three stages. During the initial discharge, two cells exhibit similar voltage profiles (Fig. 4b), whereas the i-Li evolves toward the graphite anode (Fig. 4b, stage I). As the discharge continues, the voltage of the NMC–G cell with i-Li becomes much higher than that of the control group, indicating that the i-Li has established an electrical contact with the graphite anode (Fig. 4b, stage II). The chemical reaction between i-Li and graphite lowers the potential of the anode from lithiated graphite to metallic Li, resulting in a higher cell voltage. The reconnected i-Li participates in the following electrochemical process and contributes to the extra capacity (Fig. 4b, stage III). The successful recovery of i-Li indicates that its spatial progression is substantial (>25 µm, the thickness of polyimide membrane), which is also confirmed with scanning electron microscopy (SEM; Extended Data Fig. 6b, c).

To further demonstrate the recovery of i-Li in real battery configuration where i-Li forms directly on the anodes, we conducted Coulombic efficiency (CE) measurements with Cu–Li half cells with and without the presence of pre-formed i-Li. During the i-Li formation cycle, 5 mAh cm^{-2} of fresh Li is deposited onto Cu substrate and then stripped away, generating an average of 0.33 mAh cm^{-2} of 'dead Li' on Cu (Extended Data Fig. 7a, b). During the following cycle with a deposition capacity of 1 mAh cm^{-2}, a capacity of 1.068 mAh cm^{-2} is delivered under a stripping current of 3 mA cm^{-2}, corresponding to a CE of 106.8% (Fig. 4c). This over-100% CE is strong evidence that the pre-formed 'dead Li' is reactivated and stripped away. By contrast, under the same testing conditions without pre-formed i-Li, the Cu–Li cell exhibits a CE of 94.1% (Fig. 4c).

Furthermore, the recovery efficiency of i-Li closely correlates with the stripping current (Fig. 4d). The average CEs of Cu–Li cells with pre-formed i-Li under stripping currents between 2 and 7 mA cm^{-2}
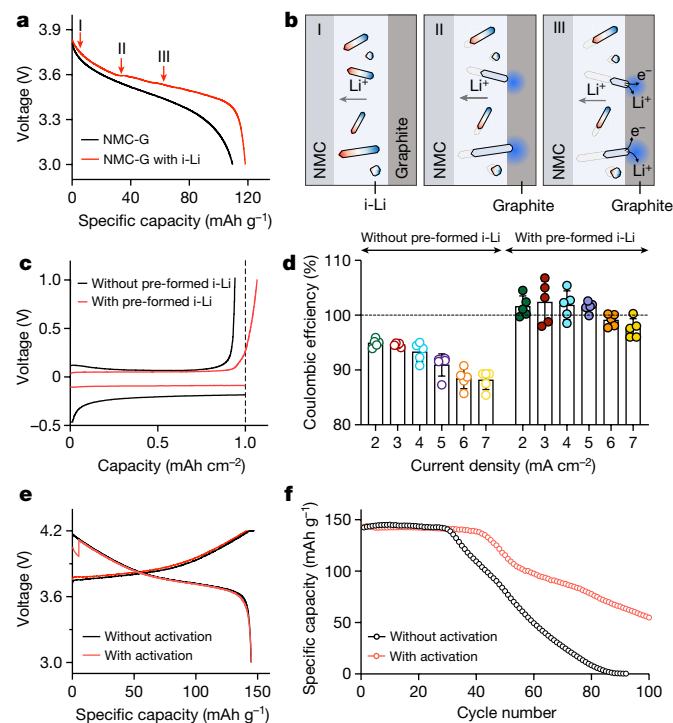
Fig. 4 | Progression and recovery of i-Li in coin cells during discharge.
a, Voltage–capacity profiles of NMC–G cells with and without i-Li. **b**, Three stages of the progression of i-Li, labelled in **a**. **c**, Voltage profiles of Cu–Li cells with and without pre-formed i-Li under a stripping current of 3 mA cm^{-2}. **d**, CEs of Cu–Li cells with and without pre-formed i-Li under different stripping currents. Each coloured circle represents the CE of one Cu–Li cell, the box shows the average CE of five cells, and the error bars indicate 1 standard deviation. The dashed line corresponds to 100% CE. **e**, Voltage–capacity profiles of a NMC–Li cell with and without activation at a rate of 1C during the first cycle. **f**, Specific capacity of NMC–Li cells with and without activation.

(in steps of 1 mA cm^{-2}) are 100.8%, 102.4%, 101.8%, 101.5%, 99.1% and 97.6%, respectively. As a comparison, the average CEs of Cu–Li cells without pre-formed i-Li under the same currents are 94.9%, 94.6%, 93.3%, 90.9%, 88.4% and 88.2%, respectively (Fig. 4b). We further calculated the recovery percentage of 'dead Li' under each current on the basis of the differences in CE. As shown in Extended Data Fig. 7c, the recovery percentage of 'dead Li' boosts from 17.6% to 31.7% when the stripping current increases from 2 to 5 mA cm^{-2}. This general trend is consistent with our simulation result, which shows that the charge transfer rates on i-Li increase with the applied current densities. A faster progression rate of i-Li leads to a higher possibility of being reconnected with the electrode. In the meantime, a higher current also leads to faster corrosion of i-Li and more Li loss. When the activation current further increases from 5 to 7 mA cm^{-2}, the recovery amount of i-Li reaches a plateau around 5–6 mA cm^{-2} and then slightly decreases to 28.3% at 7 mA cm^{-2}.

We also note that the dynamic responses of i-Li occur during every cycle, but some i-Li filaments are not reconnected during its formation cycle. The distance between i-Li and the active electrode surface (Li/current collector) can be longer than its migration distance, especially at the end of Li stripping when most of the Li filaments are dissolved. After the subsequent Li deposition, the existence of active Li filaments underneath i-Li (ref. [10]) can greatly decrease the necessary migration distance of i-Li, promoting an easier reconnection and recovery of i-Li during the second cycle. The same charging protocol is used for all cells with and without activation, and so the potential contributions from the mechanical contact between the growing Li dendrites and i-Li are eliminated.

On the basis of these results, we hypothesized that a short, fast Li-stripping step after Li deposition may promote the recovery of i-Li and extend the longevity of the Li anode. First, we compared the CE of Cu–Li cells with the presence of 'dead Li'. With an activation step at 3 mA cm^{-2} for 1 or 2 min, the CE of Cu–Li cells increases from 95.8% to 96.2% and 98.3%, respectively (Extended Data Fig. 8a–c). During the activation step, the previously generated i-Li will be polarized by the electric field and evolve toward the anode. Reconnected i-Li is stripped away during the subsequent slow-stripping process, which contributes to the increase in CE. A longer reactivation step may lead to a higher recovery efficiency of 'dead Li' but consumes more capacity in full cells. In addition, further rising the activation current to 6 mA cm^{-2} does not lead to a higher CE, owing to the faster side reactions with electrolyte (Extended Data Fig. 8d).

As a proof of concept, we evaluated the electrochemical performance of NMC–Li full cells with 150%-excessed Li with and without activation. Here we added a 2-min fast-discharging step (Li stripping) at a rate of 1C (1C = 2.67 mAh cm^{-2}) after the charging process. During this 2-min activation step, the cell delivers a specific capacity of 5.3 mAh g^{-1}, which accounts for 3.7% of its total capacity (143.1 mAh g^{-1}) (Fig. 4d). The benefit of this activation step becomes more pronounced after 30 cycles when the cell without activation starts to exhibit fast degradations in capacity (Fig. 4e) and CE (Extended Data Fig. 9a). Such degradation behaviour indicates the exhaust of excessive Li and the continuous accumulation of 'dead Li'. By sharp contrast, the cell with activation maintains stable cycling for more than 40 cycles (versus 30 cycles) and a much slower degradation process afterward. On average, the cells with activation exhibit a 29% longer cell lifetime (Extended Data Fig. 9b), which can be attributed to the partial recovery of 'dead Li'. A similar increase in cycle lifetime has also been observed under a faster-charging condition at 4 mA cm^{-2} (Extended Data Fig. 9c, d) and in the literature[29].

In this work, we demonstrate that i-Li is highly responsive to battery operations, owing to the existence of an electric field in the electrolyte. The dynamic polarization of i-Li results in its spatial progression toward the cathode (anode) during charge (discharge). By promoting its growth toward the anode through fast discharging, we further demonstrated the recovery of isolated Li in both Cu–Li and NMC–Li cells. We anticipate that the mechanistic insights into the behaviour of i-Li will inspire and guide the future development of robust lithium metal batteries and realize extreme fast-charging in lithium-ion batteries.

Online content

Any methods, additional references, Nature Research reporting summaries, source data, extended data, supplementary information, acknowledgements, peer review information; details of author contributions and competing interests; and statements of data and code availability are available at https://doi.org/10.1038/s41586-021-04168-w.

1. Bruce, P. G., Freunberger, S. A., Hardwick, L. J. & Tarascon, J.-M. Li–O₂ and Li–S batteries with high energy storage. *Nat. Mater.* **11**, 19–29 (2012); erratum *Nat. Mater.* **11**, 172 (2012).
2. Lin, D., Liu, Y. & Cui, Y. Reviving the lithium metal anode for high-energy batteries. *Nat. Nanotechnol.* **12**, 194–206 (2017).
3. Albertus, P., Babinec, S., Litzelman, S. & Newman, A. Status and challenges in enabling the lithium metal electrode for high-energy and low-cost rechargeable batteries. *Nat. Energy* **3**, 16–21 (2018).
4. Liu, J. et al. Pathways for practical high-energy long-cycling lithium metal batteries. *Nat. Energy* **4**, 180–186 (2019).
5. Cheng, X.-B., Zhang, R., Zhao, C.-Z. & Zhang, Q. Toward safe lithium metal anode in rechargeable batteries: a review. *Chem. Rev.* **117**, 10403–10473 (2017).
6. Xu, W. et al. Lithium metal anodes for rechargeable batteries. *Energy Environ. Sci.* **7**, 513–537 (2014).
7. Lu, D. et al. Failure mechanism for fast-charged lithium metal batteries with liquid electrolytes. *Adv. Energy Mater.* **5**, 1400993 (2015).
8. Niu, C. et al. High-energy lithium metal pouch cells with limited anode swelling and long stable cycles. *Nat. Energy* **4**, 551–559 (2019)
9. Yoshimatsu, I., Hirai, T. & Yamaki, J.-i. Lithium electrode morphology during cycling in lithium cells. *J. Electrochem. Soc.* **135**, 2422–2427 (1988).

10. Sanchez, A. J. et al. Plan-view operando video microscopy of Li metal anodes: identifying the coupled relationships among nucleation, morphology, and reversibility. *ACS Energy Lett.* **5**, 994–1004 (2020).

11. Gunnarsdóttir, A. B., Amanchukwu, C. V., Menkin, S. & Grey, C. P. Noninvasive in situ NMR study of "dead lithium" formation and lithium corrosion in full-cell lithium metal batteries. *J. Am. Chem. Soc.* **142**, 20814–20827 (2020).

12. Li, Y. et al. Correlating structure and function of battery interphases at atomic resolution using cryoelectron microscopy. *Joule* **2**, 2167–2177 (2018).

13. Fang, C. et al. Quantifying inactive lithium in lithium metal batteries. *Nature* **572**, 511–515 (2019).

14. Chen, K.-H. et al. Dead lithium: mass transport effects on voltage, capacity, and failure of lithium metal anodes. *J. Mater. Chem. A* **5**, 11671–11681 (2017).

15. Xu, S., Chen, K.-H., Dasgupta, N. P., Siegel, J. B. & Stefanopoulou, A. G. Evolution of dead lithium growth in lithium metal batteries: experimentally validated model of the apparent capacity loss. *J. Electrochem. Soc.* **166**, A3456–A3463 (2019).

16. Jin, C. et al. Rejuvenating dead lithium supply in lithium metal anodes by iodine redox. *Nat. Energy* **6**, 378–387 (2021).

17. Yu, Z. et al. Molecular design for electrolyte solvents enabling energy-dense and long-cycling lithium metal batteries. *Nat. Energy* **5**, 526–533 (2020).

18. Zeng, Z. et al. Non-flammable electrolytes with high salt-to-solvent ratios for Li-ion and Li-metal batteries. *Nat. Energy* **3**, 674–681 (2018).

19. Gao, Y. et al. Polymer–inorganic solid–electrolyte interphase for stable lithium metal batteries under lean electrolyte conditions. *Nat. Mater.* **18**, 384–389 (2019).

20. Weng, Y.-T. et al. An ultrathin ionomer interphase for high-efficiency lithium anode in carbonate-based electrolyte. *Nat. Commun.* **10**, 5824 (2019).

21. Lin, D. et al. Conformal lithium fluoride protection layer on three-dimensional lithium by nonhazardous gaseous reagent freon. *Nano Lett.* **17**, 3731–3737 (2017).

22. Lin, D. et al. Layered reduced graphene oxide with nanoscale interlayer gaps as a stable host for lithium metal anodes. *Nat. Nanotechnol.* **11**, 626–632 (2016).

23. Lin, D. et al. Three-dimensional stable lithium metal anode with nanoscale lithium islands embedded in ionically conductive solid matrix. *Proc. Natl Acad. Sci. USA* **114**, 4613–4618 (2017).

24. Chen, H. et al. Tortuosity effects in lithium-metal host anodes. *Joule* **4**, 938–952 (2020).

25. Mao, C., Ruther, R. E., Li, J., Du, Z. & Belharouak, I. Identifying the limiting electrode in lithium ion batteries for extreme fast charging. *Electrochem. Commun.* **97**, 37–41 (2018).

26. Belov, D. & Yang, M.-H. Investigation of the kinetic mechanism in overcharge process for Li-ion battery. *Solid State Ionics* **179**, 1816–1821 (2008).

27. Doyle, M., Fuller, T. F. & Newman, J. Modeling of galvanostatic charge and discharge of the lithium/polymer/insertion cell. *J. Electrochem. Soc.* **140**, 1526–1533 (1993).

28. Fuller, T. F., Doyle, M. & Newman, J. Simulation and optimization of the dual lithium ion insertion cell. *J. Electrochem. Soc.* **141**, 1–10 (1994).

29. Zheng, J. et al. Highly stable operation of lithium metal batteries enabled by the formation of a transient high-concentration electrolyte layer. *Adv. Energy Mater.* **6**, 1502151 (2016).

Article

Methods

Electrodes and electrolytes

$LiNi_{0.5}Mn_{0.3}Co_{0.2}O_2$ (90% NMC, 5% super P carbon, and 5% PVDF binder, mass loading: 18.57 mg cm^{-2}) coated on aluminium foil was used as NMC cathode. Graphite (91.83% graphite, 2% super P carbon, 6% PVDF binder and 0.17 % oxalic acid, mass loading: 9.38 mg cm^{-2}) coated on copper was used as graphite anode (G). High-purity Li foil (750 μm, 99.9% (Alfa Aesar)) and Cu foil (Pred Materials) were used in Cu–Li half cells. Thin Li foil laminated on the copper foil (20 μm, Hydro-Québec) was used as Li anode for NMC–Li full cell. The solution of 1-M lithium hexafluorophosphate (LiPF$_6$) in 1:1 (vol.:vol.) ethylene carbonate (EC) and diethyl carbonate (DEC) (BASF) was used as the electrolyte for NMC–G cells, and the solution of 1 M LiPF$_6$ in 1:1 (vol.:vol.) EC:DEC with 10% fluoroethylene carbonate (FEC) (BASF) and 1% vinyl ethylene carbonate (VC) (MilliporeSigma) was used as the electrolyte for NMC–Li cells and Cu–Li cells. The solution of 1-M lithium bis(fluorosulfonyl) imide (LiFSI) (Arkema) in dimethoxyethane (DME) (MilliporeSigma) was used in Cu–Li half cells.

Electrochemical testing

Without further specification, all the cells were assembled in an argon-filled glovebox with an O$_2$ level < 0.2 ppm and an H$_2$O level < 0.1 ppm, with Celgard M824 (12 μm, polypropylene–polyethylene–polypropylene) as the separator. All the cells were resting at the open-circuit voltage for 3 h before electrochemical tests. Galvanostatic charge–discharge tests with coin cells were conducted on a Land 8-channel battery tester, and other electrochemical tests with optical cells and multi-electrode PTFE cells were performed on a Biologic VMP3 system. NMC–Li cells and NMC–G cells were cycled between 3–4.2 V, and their C rate and specific capacity were calculated based on the mass loadings of the NMC cathode. The prototype NMC–Li full cells were charged under a constant current density of 0.8 mA cm^{-2} (0.3C rate) and followed by a constant voltage charging at 4.2 V (cut-off current: 0.268 mA cm^{-2}). The discharging process was conducted under a constant current density of 0.268 mA cm^{-2} (0.1C rate).

In Cu–Li half cells, both the Li and Cu foils were punched to 1 cm^2. Cu was rinsed with 0.1 M HCl, deionized water, ethanol (Fisher) and acetone (Fisher) to remove surface contaminants. Lithium was mechanically sheared with a polyethylene scraper to remove the surface oxide. After 1-h rest at open-circuit voltage, ten pre-cycles between 0 and 1 V were conducted at 0.1 mA cm^{-2} before CE measurements. These ten cycles were conducted to reduce the oxides on the Cu surface and form an initial SEI layer to improve the experimental consistency. The Cu substrates remained a shiny copper colour after cycling, and we did not observe any i-Li on the surface. During the i-Li formation cycle, 5 mAh cm^{-2} of fresh Li was deposited onto Cu substrate and stripped away, both under a current density of 5 mA cm^{-2}. During the following cycle, another 1 mAh cm^{-2} of fresh Li was deposited onto Cu substrate at 5 mA cm^{-2} and stripped away under various current densities until the cut-off voltage of 1 V. For the control cells without the pre-formed i-Li, the i-Li formation cycle is not conducted, and all the other conditions are maintained as the same.

Fabrication and assembly of optical cells

Glass slides were used as the substrates for optical cells. Copper microelectrodes with a size 100-μm wide and 500-μm long were patterned on glass slides using photolithography (ML3 MicroWriter). The metal evaporation process was conducted with an e-beam evaporator (KJ Lesker) with a base pressure below 10^{-6} torr. Titanium (5 nm) was deposited first as an adhesion layer, and subsequently, 50 nm of copper was deposited above it. All the patterned glass slides were cleaned with acetone (Alfa Aesar) and 2-propanol (Alfa Aesar) and dried under vacuum at room temperature. NMC cathode and Li anode were pre-cut into a square shape with a length of 3 mm and aligned in parallel with the copper microelectrode in the middle. The distance between the NMC cathode and the Li anode is around 1–2 mm, which is limited by the cell assembly process in the glovebox. The electrolyte was injected into the cell with a syringe. The optical cell was covered with a cover glass (1 cm^2 in size, 145-μm thick, Alfa Aersa), and the edges were sealed with epoxy.

Electrochemical testing of optical cells

During Li deposition, the Cu microelectrode was employed as the working electrode, and the Li electrode was used as the counter electrode. The electrodeposition process was conducted under a current of 100 μA for 2 h, and Li was homogenously deposited onto the Cu substrate exhibiting a dendritic morphology. Then this Cu/Li electrode was disconnected from the external circuit and deployed as an electrically isolated Li island. The charging/discharging process of the NMC–Li cell was conducted at 5 μA. The electrochemical tests were paused during the acquisition of optical images to ensure image quality.

Material characterization

An FEI Magellan 400 XHR scanning electron microscope was used for SEM. Samples were exposed to air for less than 5 s during the transfer process. The XPS profiles were collected with a PHI VersaProbe 1 scanning XPS microprobe and samples were transferred in a transfer vessel without exposure to air.

Numerical simulation

The framework of this electrochemical model is established based on the theory developed in refs. [27,28]. A deformed geometry modulus is added to the model and coupled with the electrochemical modulus to track the morphological evolution of the isolated Li islands. All the numerical simulation is performed using COMSOL Multiphysics software. The geometrical and electrochemical parameters in the numerical model are set to be consistent with the experimental setup.

In the electrochemical model, the electric current in the electrolyte ($\mathbf{i}_l$) is governed by the diffusion and migration of Li$^+$, and can be described as:

$$\mathbf{i}_l = (-K_l \nabla \phi_l) + \frac{2K_l RT}{F}\left(1 + \frac{\partial \ln f}{\partial \ln C_l}\right)(1 - t_+)\nabla \ln C_l, \qquad (2)$$

where K_l is the ionic conductivity of the electrolyte, C_l is the concentration of Li$^+$ in the electrolyte, R is the gas constant, T is the temperature, F is Faraday's constant, t_+ is the transference number of Li$^+$, and f is the mean molar activity coefficient of the electrolyte (Extended Data Table 1). The Butler–Volmer equation is used to describe the relationship between the charge transfer rate (i) and the overpotential (η),

$$i = i_0\left(\exp\left(\frac{\alpha_a F\eta}{RT}\right) - \exp\left(-\frac{\alpha_c F\eta}{RT}\right)\right), \qquad (3)$$

where α_a (α_c) is the anodic (cathodic) transfer coefficient (Extended Data Table 1), and i_0 is the exchange current density. The mass transport of Li$^+$ in the electrolyte is defined as

$$\frac{\partial C_l}{\partial t} + \nabla \cdot \mathbf{J}_l = 0, \qquad (4)$$

$$\mathbf{J}_l = -D_l \nabla C_l + \frac{\mathbf{i}_l t_+}{F}, \qquad (5)$$

where $\mathbf{J}_l$ represents the Li$^+$ flux in the electrolyte, and D_l is the Li$^+$ diffusivity in the electrolyte.

The exchange current density i_0 is defined as:

$$i_0 = F(k_c)^{\alpha_a}(k_a)^{\alpha_c}(C_{S_{max}} - C_S)^{\alpha_a}(C_S)^{\alpha_c}\left(\frac{C_l}{C_{l_{ref}}}\right)^{\alpha_a}, \qquad (6)$$

where k_c (k_a) is the rate constant for the anodic (cathodic) reactions, C_s is the bulk Li$^+$ concentration in the active material, $C_{s_{max}}$ is the maximum Li$^+$ concentration in the active material, and $C_{l_{ref}}$ is a reference Li$^+$ concentration in the electrolyte.

At the Li/electrolyte interface, equations (1), (6) can be simplified as follows:

$$\eta = \phi_{s(Li)} - \phi_l,\tag{7}$$

$$i_0 = F(k_c)^{\alpha_a}(k_a)^{\alpha_c}\left(\frac{C_l}{C_{l_{ref}}}\right)^{\alpha_a}.\tag{8}$$

The electric current density in an NMC cathode $\mathbf{i}_c$ at a given location is defined by Ohm's law,

$$\mathbf{i}_c = -K_c\nabla\phi_{s(NMC)},\tag{9}$$

where K_c is the electric conductivity and $\phi_{s(NMC)}$ is electric potential of an NMC cathode.

Owing to the charge conservation, the electric current density field follows

$$\nabla\cdot\mathbf{i}_c = 0, \text{ and} \nabla\cdot\mathbf{i}_l = 0.\tag{10}$$

The boundary conditions for the electric field used in the half-cell model are:

$$\mathbf{i}_l\cdot\mathbf{n}_{side} = 0, \text{ at the lateral boundaries of half-cell model,}$$
$$\mathbf{i}_c\cdot\mathbf{n}_{side} = 0, \text{ at the lateral boundaries of half-cell model,}$$
$$\mathbf{i}_l\cdot\mathbf{n}_{cc} = 0, \text{ at the cathode current collector,}$$
$$\mathbf{i}_c\cdot\mathbf{n}_{cc} = -i_{app}, \text{ at the cathode current collector,}$$
$$\phi_{s(Li)} = 0, \text{ at the surface of the Li metal anode,}$$

<div style="text-align:right">(11)</div>

where $\mathbf{n}_{side}$ is the unit normal vector pointing outside from the model, $\mathbf{n}_{cc}$ is the unit normal vector pointing from the cathode to the current collector, and i_{app} is the applied current density at the current collector.

The mass transport of Li$^+$ in the active materials can be described as

$$\frac{\partial C_s}{\partial t} + \nabla\cdot\mathbf{J}_s = 0,$$

$$\mathbf{J}_s = -D_s(\nabla C_s),\tag{12}$$

where $\mathbf{J}_s$ represents Li$^+$ flux in the active material and D_s represents the Li$^+$ diffusivity in the active materials.

The boundary conditions in the half-cell model are as follows,

$$\mathbf{J}_l\cdot\mathbf{n}_{side} = 0, \text{ at the lateral boundaries of the half-cell model,}$$
$$\mathbf{J}_s\cdot\mathbf{n}_{side} = 0, \text{ at the lateral boundaries of the half-cell model,}$$
$$\mathbf{J}_l\cdot\mathbf{n}_{cc} = 0, \text{ at the cathode current collector,}$$
$$\mathbf{J}_l\cdot\mathbf{n}_{Li} = \frac{i_{app}}{F}, \text{ at the surface of the Li metal anode.}$$

<div style="text-align:right">(13)</div>

Initial concentration of Li$^+$ in the electrolyte and active material are given as $C_{l_{ini}}$ and $C_{s_{ini}}$ at $t = 0$. All the parameters in the numerical model are listed in Extended Data Table 1.

Data availability
All the data that support the findings of this study are available from the corresponding author upon request. Source data are provided with this paper.
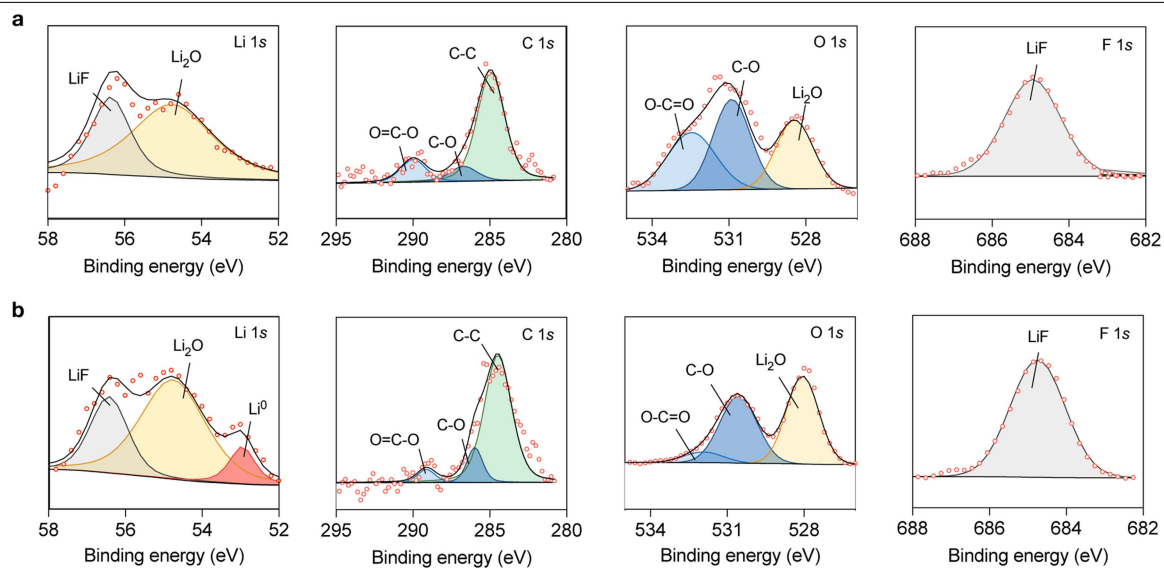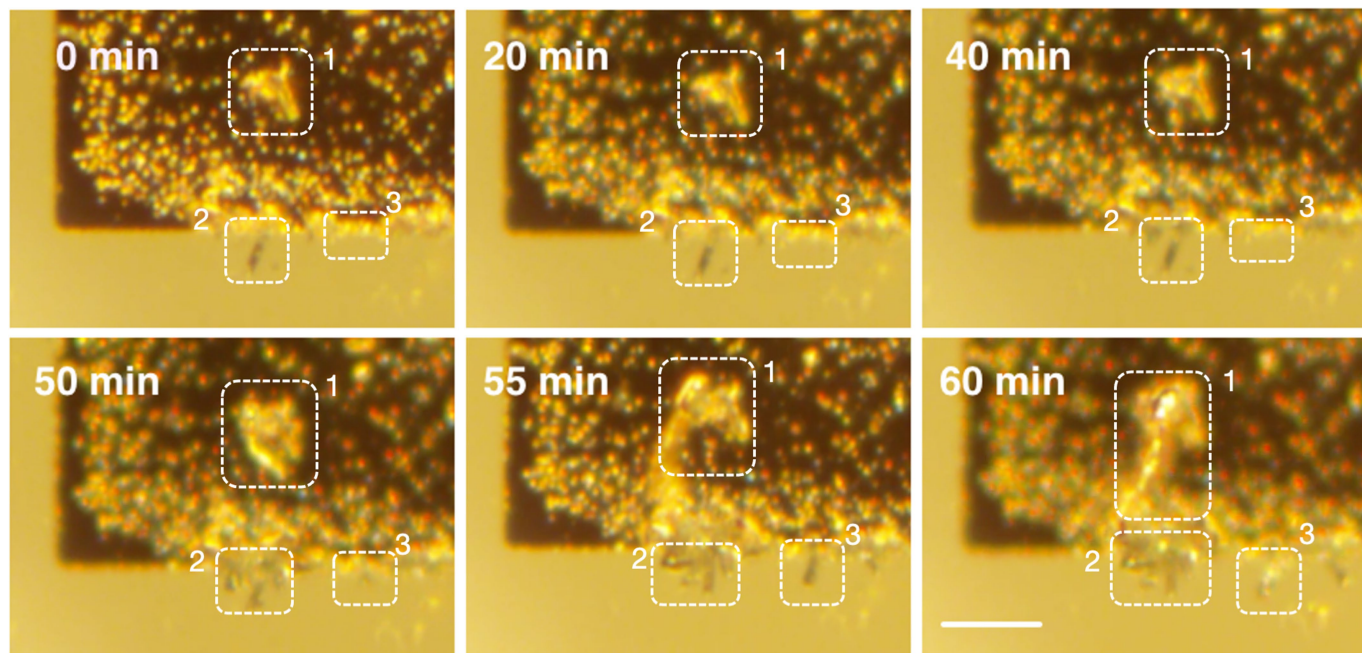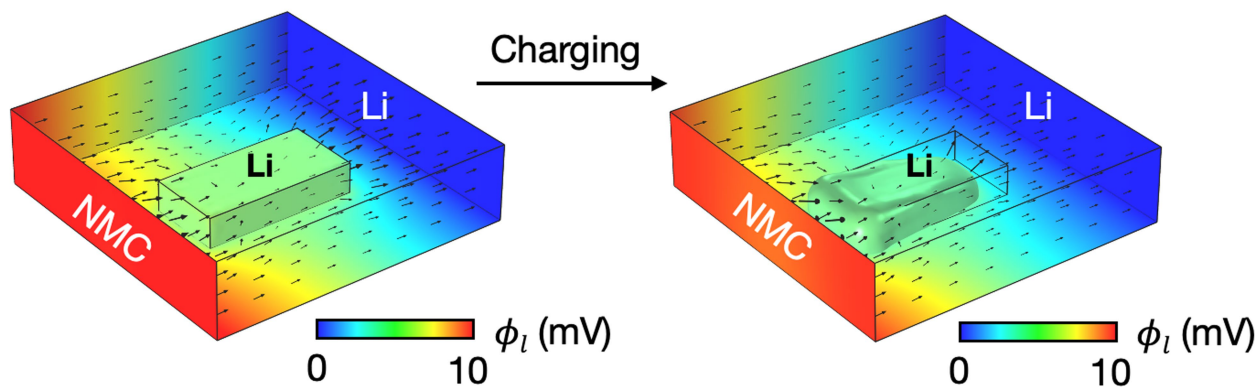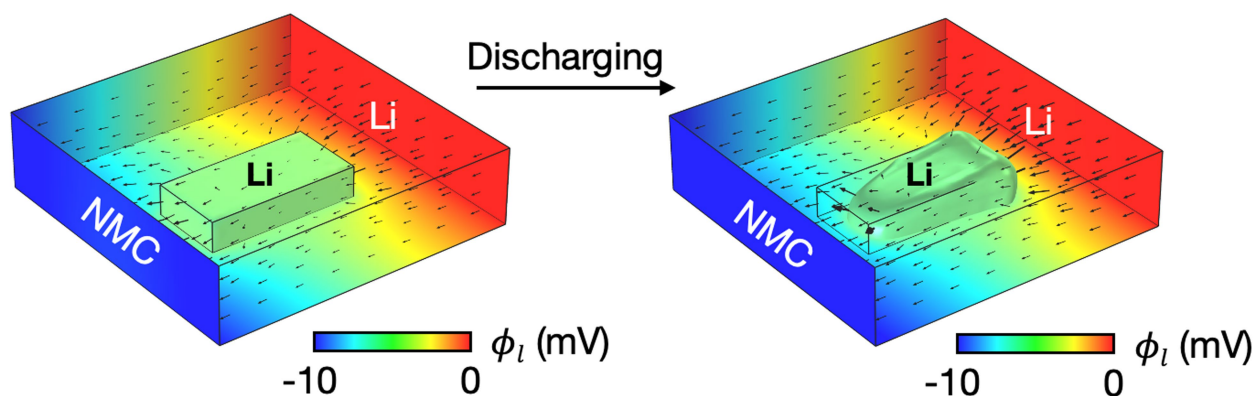
Extended Data Fig. 1 | Configuration of optical cells with i-Li island between electrodes. a, Experimental setup. **b**, Optical image of the deposited lithium on the Cu island. The scale bar is 100 μm.
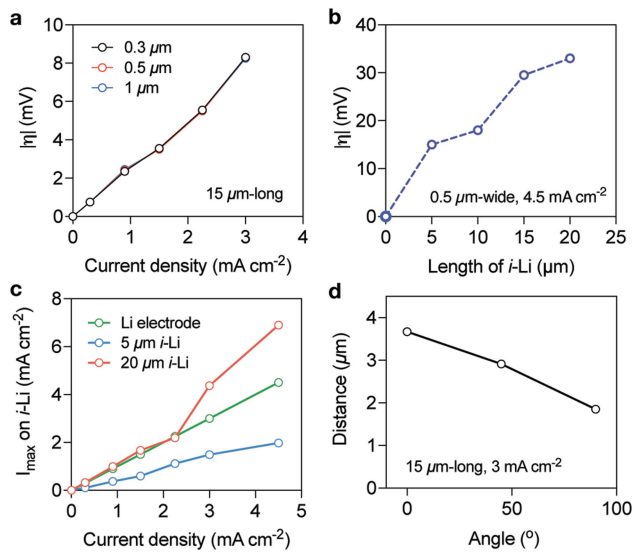
Extended Data Fig. 2 | Compositional evolution on i-Li island during charge. a, **b**, X-ray photoelectron spectroscopy analysis of the ends of i-Li island near Li anode (**a**) and NMC cathode (**b**) after 3 h charging.
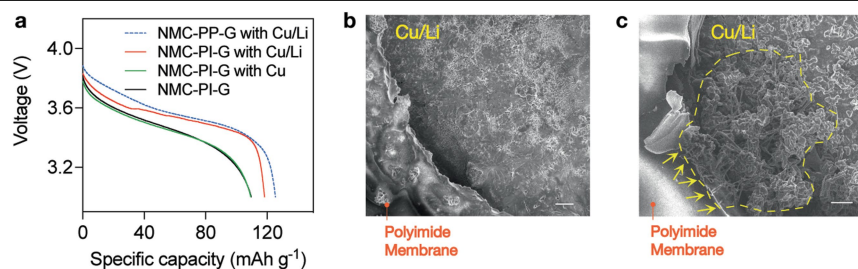
Extended Data Fig. 3 | Morphological evolution of 'dead Li' during charge. Optical images showing the evolution process of micrometre-sized, electrochemically generated 'dead Li' filaments under a charging current of 20 µA. The scale bar is 20 µm.

Extended Data Fig. 4 | Potential distributions in the electrolyte during battery operations. a, **b**, The potential distribution in the electrolyte during charge (**a**) and discharge (**b**). The direction of Li$^+$ flux is shown in black arrows. The initial and end states are at $t = 100$ s and 2 h, respectively.
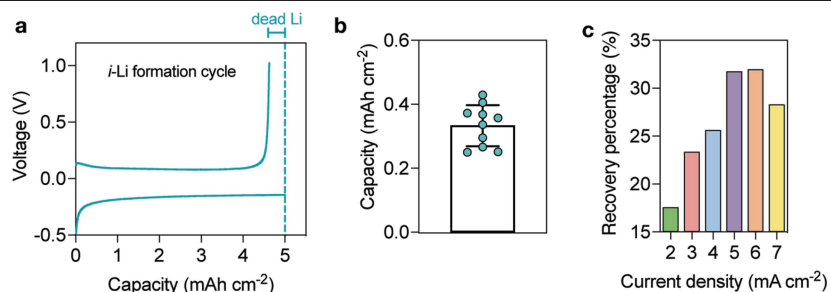
Extended Data Fig. 5 | The dynamic response and spatial progression of i-Li during battery operations. a, **b**, The absolute overpotentials at two ends of i-Li with different width (**a**) and length (**b**) during charge. **c**, The maximum current densities at the ends of i-Li filaments and Li electrode under various current densities during discharge. **d**, The migration distance of i-Li with different orientations at the end of 1C discharge (1C = 3 mA cm⁻²). The orientation of i-Li is defined as the angle between i-Li and the electric field. 0° and 90° represent the directions along and perpendicular to the electric field, respectively.

Extended Data Fig. 6 | Progression of i-Li in coin cells during discharge.
a, Voltage–capacity profiles of NMC–G cells with different cell configurations. NMC–polyimide (PI)–G cells with/without Cu present identical voltage profiles, indicating that the addition of Cu does not influence the electrochemical performance of NMC–G cell. Red arrow marks the voltage fluctuation observed in NMC–PI–G cell with Cu/Li due to i-Li's progression. Meanwhile, the NMC–poly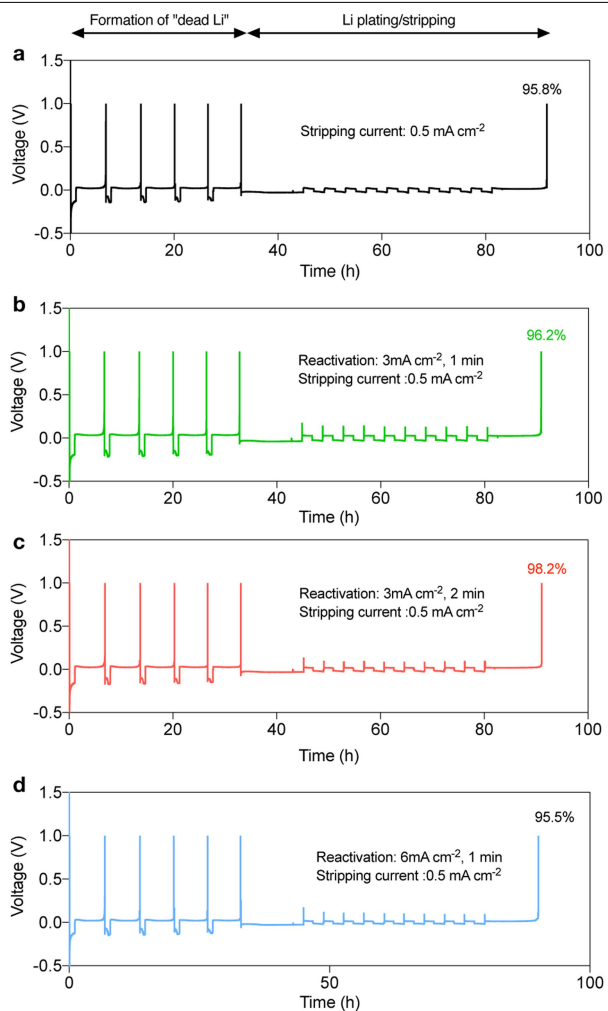propylene–G cell with i-Li (Cu/Li) exhibits a smooth voltage profile, suggesting that i-Li could not penetrate through the nano-sized pores of commercial polypropylene (PP) separators. **b**, **c**, SEM images of Cu/Li (bottom) and polyimide membrane (top) after 5-min (**b**) and 1-h charge (**c**), showing that i-Li penetrates through the polyimide membrane. Arrows point out the Li dendrites on the edge of polyimide membrane. The scale bars are 10 μm.
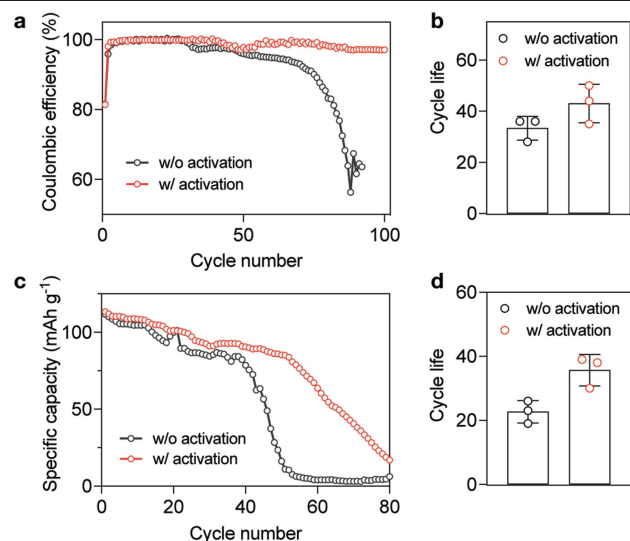
a, A representative voltage profile of Cu–Li cell during i-Li formation cycle.
b, Capacity of 'dead Li' on average. Each coloured sphere represents the CE of one Cu–Li cell, the box shows the average CE of ten cells, and the error bar illustrates 1 standard deviation. **c**, The recovery percentage of 'dead Li' under different stripping currents.

Extended Data Fig. 7 | The recovery of 'dead Li;' during discharge.

Extended Data Fig. 8 | Coulombic efficiency measurements of Cu–Li half-cells with/without activation in the presence of 'dead Li'. a–d, The stripping conditions are 0.5 mA cm^{-2} with an activation step of **a**, none, **b**, 3 mA cm^{-2} for 1 min, **c**, 3 mA cm^{-2} for 2 mins, and **d**, 6 mA cm^{-2} for 1 min. For the average CE measurement, a standard protocol is followed: (1) 5 mAh cm^{-2} of Li is deposited onto Cu under 0.5 mA cm^{-2} as a Li reservoir, (2) repeatedly deposit 1 mAh cm^{-2} of Li (0.5 mA cm^{-2}) and strip under different conditions for ten cycles, (3) strip all active Li (0.5 mA cm^{-2}) until 1 V. Accumulated 'dead Li' are formed by 5 cycles of Li deposition (3 mA cm^{-2}, 1 h) and stripping (0.5 mA cm^{-2} until 1 V).

Extended Data Fig. 9 | Electrochemical performance of NMC–Li cells with/ without activation. a, Coulombic efficiency and **b**, cycle life of NMC–Li cells (150%-excessed Li) with/without activation. **c**, Specific capacity and **d**, cycle life of NMC–Li cells (300%-excessed Li) under a fast-charging condition. Each coloured sphere represents the cycle life of one NMC–Li cell, the box shows the average cycle life of three cells, and the error bar illustrates 1 standard deviation. Cycle life is defined as the cycle number when the cell capacity falls below 80% of its initial capacity. TF stands for temperature fluctuation.

Extended Data Table 1 | Parameters used in the numerical modelling

Parameter (unit)	Value	Parameter (unit)	Value
Electric conductivity of carbon-binder matrix, K_c (S/m)	10^4	Equilibrium potential for Li reaction in NMC, E_{eq} (V)	$4.4-2.8y+8.2y^2+9.8\,y^3-214.5y^4+777.8y^5-1290.6y^6+1034.4y^7-324.2y^8$, $y = C_s/C_{s\_max}$
Electric conductivity of electrolyte, K_l (S/m)	1.147		
Transference number of cations, t_+	0.363	Li ion diffusivity in electrolyte, D_l (m^2/s)	1×10^{-10}
molar activity coefficient of electrolyte, $\partial \ln f / \partial \ln C_l$	0.43	Li diffusivity in active materials, D_s (m^2/s)	7×10^{-15}
Rate constant for cathodic reaction, k_c (m/s)	2×10^{-11}	Initial Li ion concentration in electrolyte, C_{l_ini} (mol/m^3)	1000
Rate constant for anodic reaction, k_a (m/s)	2×10^{-11}	Max. Li concentration in active materials C_{s_max} (mol/m^3)	48700
Cathodic transfer coefficient, a_c	0.5	Density of metallic lithium, ρ (kg/m^3)	534
Anodic transfer coefficient, a_a	0.5	Molar mass of metallic lithium, M_{Li} (kg/mol)	0.006941
Porosity of NMC cathode, e_c	0.5	Porosity of separator, e_s	0.4